A New Mathematical Model for Monitoring the Temporal Evolution of the Ice Crystal Size Distribution during Freezing in Pharmaceutical Solutions

Domenico Colucci[a,b*], Davide Fissore[a], Antonello A. Barresi[a], Richard D. Braatz[b]

[a] Dipartimento di Scienza Applicata e Tecnologia. Politecnico di Torino, Corso Duca degli Abruzzi 24, 10129 Torino, Italy.

[b] Department of Chemical Engineering, Massachusetts Institute of Technology, 77 Massachusetts Avenue, 02139, Cambridge, MA, USA.

*Corresponding author

Email: domenico.colucci@polito.it

Tel: 0039 011 090 4695

1

Abstract

The freezing step plays a key role in the overall economy of the vacuum freeze-drying of pharmaceuticals, since the nucleation and crystal growth kinetics determine the number and size distribution of the crystals formed. In this work, a new mathematical model of the freezing step of a (bio)pharmaceutical solution is developed and validated. Both nucleation and crystal growth kinetics are modeled and included in a one-dimensional population balance (1D-PBM) that describes, given the product temperature measurement, the evolution of the pore size distribution during freezing. The developed model is coupled with the real-time measurements obtained from an infrared video camera. The ending time of the primary drying stage, and the maximum temperature inside the material, simulated through a simplified model of the process and the pore distribution forecast, resulted in good agreement with experimental values. The resulting Process Analytical Technology (PAT) has the potential to boost the development and optimization of a freeze-drying cycle and the implementation of a physically grounded Quality-by-Design approach in the manufacturing of pharmaceuticals. A more general mathematical model, including the aforementioned population balance, of a vial filled with a solution of sucrose was also developed and used to further validate the approach.

Keywords:

Mathematical modeling; Freezing; Crystal size distribution; Master equation.

2

1. Introduction

Freeze drying is a low-temperature drying process, particularly appreciated in comparison to other drying processes, as it avoids damage to thermally sensitive Active Pharmaceutical Ingredients (API). In a typical freeze-drying cycle, the liquid formulation is first poured into single-dose containers and frozen, by cooling the shelves upon which the vials are placed. Cooling a sample below its equilibration freezing point induces crystallization of the solvent, typically water, in the liquid formulation. Some of the original solvent remains in a liquid state, bounded to the solid structure. Solvent removal is carried out in two phases, namely, primary and secondary drying. In the former, the pressure is reduced below the triple point of water, while the temperature of the shelves is increased to allow the sublimation of the ice crystals formed; in the latter, since the amount of bound water is usually greater than the allowed residual moisture content in the final product, the temperature is further raised to enhance its desorption [1-4].

In recent years, the number of drugs and pharmaceutical products that require a freeze-drying step in the manufacturing process, for solvent removal and drug stabilization, has increased. Also the requirements in terms of efficiency, quality, and safety have become more stringent, which has motivated efforts to improve the understanding and design of the freezing process [5],[6]. During the subsequent drying, ice crystals will sublime to leave voids within a porous network through which the water vapor will flow on its way from the sublimation interface to the drying chamber. Structure characterized by bigger pores enables a higher sublimation flux [7], due to the lower transport resistance of the dried product, while having an opposite effect on the rate of the secondary drying, because of a lower surface-area-to-volume ratio [8]. As the porous structure directly influences the mass transfer rates, and product temperature results from a thermal balance between the heat transferred to the product and the heat removed through sublimation, the porous structure also affects the spatial temperature distribution during the drying stages. The temperature of the product is a critical variable that

3

must be carefully monitored to avoid jeopardizing product quality or impairing the APIs. The formation of small ice crystals, increasing the interfacial area, might also affect the unfolding and aggregation of proteins [9].

The prediction of the crystal size distribution resulting from the freezing of the liquid formulation is of utmost importance for process optimization, not only in the freeze drying of pharmaceutical solutions, and has been deeply investigated in the past years. In the literature, many empirical relationships can be found to correlate the thermal evolution of the product to the average pore size. Bald [10] first proposed to relate mean pore diameter to the cooling rate of the product by

$$\bar{D}_{p,i} = \alpha \left(\frac{dT}{dt} \right)^{-\beta} \tag{1}$$

where α and β are empirical constants that must be fitted to experimental results.

A whole family of empirical models is also available in the literature which relates the average pore diameter to the velocity of the solidification front, P, and the temperature gradient in the solid layer, Q:

$$\bar{D}_{p,i} = \alpha' P^{-\lambda_1} Q^{-\lambda_2} \tag{2}$$

where α', λ_1 and λ_2 have to be determined experimentally. In fact, the parameter Q is representative of the rate of removal of the latent heat released during crystal formation, the resulting crystal structures are dependent from this. The freezing front velocity instead is representative of the salt rejection rate at the crystals interface which is one of the phenomena governing crystal growth. A non-exhaustive list of applications of Eq. (2) includes freezing of apples [11], starch gels [12], gelatin gels [13], solidification of metal samples at low rates [14] and solidification of alloys at high rate [15]. Eq. (2), with $\lambda_1 = \lambda_2 = 0.5$, has been also used to describe the freezing of aqueous solutions in vials [16-19]. In the latter case, P and Q are calculated from

4

$$P(t) = \frac{dL_{frozen}(t)}{dt} \tag{3}$$

$$Q(t) = \frac{T_f - T_B(t)}{L_{frozen}(t)} \tag{4}$$

The strong dependence of the many parameters on the kind of product, the specific application, and operating conditions that appear in these empirical models limits the predictive reliability and accuracy of the model. Besides, the parameters P and Q provide a macroscopic description of some of the many aspects related to the dynamics of the system. They are consistent with the physics of the system, but they do not provide a characterization of the system which can be given only in terms of thermodynamic state functions.

The state of the art in the modeling of the dependency of the average pore diameter on the thermal evolution of the product is the mechanistic model proposed by Arsiccio et al. [20]. The basic idea underlying their approach is that crystal growth is an exothermic process: the incorporation of new water molecules to the existing crystals, together with the creation of new interfaces, will release energy. The cooling medium and surrounding environment remove some of this energy and, thus, an energy balance in an infinitesimal slice of the material is related to the associated crystal growth dynamics. This approach neglects the nucleation kinetics and, as all the other models previously discussed, can predict the average pore diameter but not the pore size distribution.

In this work, a different approach to modeling the freeze-drying process is proposed and validated. The nucleation kinetics is described by a stochastic model in the form of a chemical Master equation. The parameters of the nucleation kinetics are fit to achieve the best agreement between the simulated and experimental induction times. Given the number and probability distribution function of the ice seed crystals formed, their evolution over time is described by a 1D population balance. The crystal growth rate is modelled as a function of the thermodynamically correct driving force, which is the supersaturation. This model does not

5

require any additional variables to be estimated or measured; whenever a single or multiple measurement of the temperature inside the material is provided [21], the model can be solved and both the whole pore size distribution and the amount of bound water can be determined. An analytical solution of the proposed model is derived using the Method of Characteristics [22], making this approach suitable for on-line monitoring and optimization of the whole freeze-drying process.

The paper is thus organized in five more sections. Section 2 describes the stochastic model and the experimental studies performed to derive the nucleation kinetic parameters, while Section 3 presents the 1D population balance model, the assumptions made, and the derivation of the analytical solution. Chapter 4 presents the experimental setup and the case study discussed. Chapter 5 describes the methodology for the validation of the proposed model, including the mathematical simulation of the whole freezing step of a single dose container (the 2D model used is presented in Appendix A), while Chapter 6 presents the main results of the study. Chapter 7 discusses the main conclusions and future development of the proposed approach.

2. Nucleation Kinetics

During nucleation, water molecules in the liquid become aligned and solidify to form crystal nuclei that will subsequently grow to form ice crystals with a range of sizes described by a crystal size distribution. This primary nucleation phenomenon is highly stochastic, resulting in different nucleation induction times in different vials and from one experiment to the next – even if the exact same solutions and the same amount are placed in the vials. In addition, the temperature during supercooling at which ice nuclei are observed to form in a vial is much higher than in pure water (which is about -37°C) because many factors, e.g. impurities inside the vial, gas dissolved in the solution, or any particulate, might act as a center for nucleation.

6

The higher the supercooling degree, the higher the number of crystal nuclei formed, and the smaller the average diameter of the resulting pores at the end of the drying stage. In a laboratory batch freeze-drying process, the vials could nucleate in the range −10°C to −15°C; but nucleation can occur below −20°C in a clean environment using Good Manufacturing Practice (GMP) conditions. Once the nucleation process starts, ice is formed quickly and the whole vial can change its optical properties due to the appearance of the nuclei in less than one second [23].

In this work, the volumetric nucleation rate is described by

$$B_0 = k_b \left(T_f - T \right)^b \tag{5}$$

where T_f is the equilibrium freezing temperature, and the prefactor k_b and exponent b are parameters that must be experimentally estimated. The driving force in this system is the difference between the actual temperature of the solution, T, measured in this work using the infrared camera, and the equilibrium temperature since, until the moment the first nucleus is formed, temperature is the only physical property of the system changing with time.

During cooling, the induction time is the time elapsed between the moment the solution reaches the equilibrium freezing temperature and the appearance of the first ice crystal. The common practice in the crystallization literature is to fit the parameters in the nucleation rate expression to experimentally measured induction times. Deterministic population balances and moment equations can hardly capture the intrinsically stochastic nature of nucleation. The induction times follow a probability distribution, which has been modeled using Gamma [24] and Poisson [25,26] distributions in case of supersaturation (and nucleation rate) kept constant over time. When supersaturation is time varying, as in our system, the nucleation rate increases as the solution is cooled. Goh et al. [27] modelled the stochastic nucleation process as a series of nonstationary Poisson events, which defines a chemical Master equation whose solution predicts the induction time distribution for any form of the nucleation rate and supersaturation

7

profile. Analytical solutions were derived for the time-varying probability of crystal nucleation, the average number of crystals that form at any certain time t, and the induction time statistics. Two assumptions are made: (i) the time for a nucleus to grow to a size sufficient to become experimentally observed is negligible and (ii) the solution remains spatially uniform after nucleation, that is, the depletion rate of the solution is not large enough to induce spatial non-uniformity in the system. Assumption (i) holds for nearly any primary nucleation process, including our system, because the growth rate is nearly always high at the high supersaturation at which the first nucleus forms. Assumption (ii) only affects the dynamics after the first nucleus forms, and so does not affect the analytical expression for the induction time distribution used in this article.

The nucleation rate in the chemical Master equation is represented by

$$K(t) = k_b \left(T_f - T(t)\right)^b V = k_b \left(\Delta T(t)\right)^b V \tag{6}$$

where, since $K(t)$ describes the number of nuclei formed per second, $K(t)dt$ will represent the probability to observe the formation of a stable nucleus during the time interval dt. The analytical expression for the induction time distribution is [27];

$$f\left(t_{ind}|k_b,b\right) = K(t_{ind}) \exp\left(-\int_{t_{sat}}^{t_{ind}} K(s)ds\right) \tag{7}$$

Inserting Eq. (6) into this expression gives

$$f\left(t_{ind}|k_b,b\right) = k_b \left(\Delta T(t_{ind})\right)^b V \exp\left(-\int_{t_{sat}}^{t_{ind}} k_b \left(\Delta T(s)\right)^b V ds\right), \tag{8}$$

By the definition of induction time, the probability of having one nucleus, i.e. the integral of $K(t)dt$ between the saturation time and the induction time, must assume a unitary value, thus the two kinetic parameters, k_b and b, are related and cannot be optimized individually, that is given b, for the previous constrain, the value of k_b will also be fixed. The natural logarithm of

8

the likelihood function for k_b, given a specified certain value b, can be derived from Eq. (7) to be

$$\ln L\left(k_b|t_i\right) = \ln \prod_{i=1}^{N} f\left(t_i|k_b\right) = \sum_{i=1}^{N} \ln\left(f\left(t_i|k_b\right)\right) = \sum_{i=1}^{N} \ln K(t_i) - \sum_{i=1}^{N} \int_{t_{sat}}^{t_i} K_i(s)ds \qquad (9)$$

where t_i is the ith measured induction time. Setting the derivative equal to zero it is possible to determine the maximum of the likelihood function that, inserting from Eq. (6), results in

$$\frac{d \ln L\left(k_b|t_i\right)}{dk_b} = \frac{N}{k_b} - V \sum_{i=1}^{N} \int_{t_{sat}}^{t_i} \left(\Delta T(s)\right)^b ds = 0, \qquad (10)$$

which can be rearranged to give an analytical expression for the prefactor,

$$k_b = \frac{N}{V \sum_{i=1}^{N} \int_{t_{sat}}^{t_i} \left(\Delta T(s)\right)^b ds}. \qquad (11)$$

A simple algorithm for the determination of the maximum-likelihood parameter estimates is to test all the exponents b in a reasonable interval, e.g. between 1 and 10 [28]. The best value of b is searched for and k_b computed using Eq. (11), which can be inserted into Eq. (8) to give the predicted induction time distribution for any experimental supercooling profile. The measured induction times were fitted to the mode obtained from the induction time distribution in Eq. (8), e.g., to minimize the least-squares-error Ψ_b defined by

$$\Psi_b = \sum_{i=1}^{N} (t_{i,\text{mod}} - t_{i,\text{measured}})^2. \qquad (12)$$

The variation in the measured induction times can be characterized by the standard deviation of the induction time distribution. The reader might refer to the original paper by Goh et al. [27] for a clear and detailed description of the model and for its derivation.

3. Crystal Size Distribution Modeling and Prediction

9

The conservation equation for the number of particles is a population balance model (PBM) [29,30]. This framework is sufficiently general to model the dynamics of formation, growth, breakage, and aggregation of many particles.

In our case, since the system is at rest, crystal breakage and crystal aggregation are negligible. Secondary nucleation terms were also neglected. A one-dimensional population balance (1D-PBM) for a population of crystals, assumed to have a characteristic length scale L that encompasses only growth is

$$\frac{\partial n(L,t)}{\partial t} + \frac{\partial \left(G(L,t) n(L,t) \right)}{\partial L} = 0 \tag{13}$$

where G is the growth rate and n the normal distribution function, that is the number of crystals in an infinitesimal volume of the property space. The growth rate is assumed proportional to the surface area of the single crystals and to a driving force, defined as the difference of the chemical potential between the ice and the solution:

$$G(L,t) = k_{cg} \sigma^g A_{crystals} \tag{14}$$

For example, if the ice crystals were assumed to be cylindrical, and the surface of the top of the cylinders were neglected, then

$$A_{crystals} = 2\pi L \Delta z + 2\pi L^2 \approx 2\pi \Delta z L \tag{15}$$

and

$$G(L,t) = k_{cg} \sigma^g 2\pi \Delta z L = G'(t) L \tag{16}$$

The non-dimensional difference between the chemical potentials is

$$\sigma = \frac{\mu_{w,i} - \mu_{w,l}}{RT} = \ln \frac{a_w^i}{a_w^l} \tag{17}$$

The logarithm of the activity of ice was calculated from [31]

$$\ln a_w^i = \frac{\Delta H_{fus}^0}{R} \left(\frac{1}{T_1^0} - \frac{1}{T} \right) - \frac{\Delta c_{p,l}^0}{R} \left(\ln \frac{T_1^0}{T} + 1 - \frac{T_1^0}{T} \right) \tag{18}$$

10

where the apex "0" identifies the standard condition at which the ice properties are referred.

A UNIQUAC model was used to determine the liquid activity while correctly accounting for the effect of concentration due to solvent crystallization:

$$\ln a_w^l = \ln \gamma_w x_w = \ln \gamma_w + \ln x_w \tag{19}$$

$$\ln \gamma_w = \ln \left(\frac{w_i}{x_i} \right) + 1 - \frac{w_i}{x_i} + q_i \left[1 + \ln \sum_i \left(\theta_j \tau_{ij} \right) - \sum_j \frac{\theta_j \tau_{ij}}{\sum_k \theta_k \tau_{kj}} \right] \tag{20}$$

The parameters for the UNIQUAC model for a sucrose solution were taken from Catté et al. [32] and are reported in Table 1.

Substitution of Eq. (16) into Eq. (13) gives

$$\frac{\partial n(L,t)}{\partial t} + G(L,t) \frac{\partial n(L,t)}{\partial L} = -n(L,t) G'(t) \tag{21}$$

Eq. (21) was solved with the conditions

$$\boldsymbol{n} = \boldsymbol{O}, \ \forall L, \forall t < t_{ind} \tag{22}$$

$$n = \frac{B_0(t)}{G'(t)} B(\beta_1, \beta_2), \ L = L_0, t = t_{ind} \tag{23}$$

The first condition (22) indicates that there are no crystals in the vial until the first nuclei form. The second condition provides the initial distribution function for the ice seeds created when the conditions for nucleation are met. The ice crystals are assumed to be distributed according a Beta distribution (B) with parameters β_1 and β_2. This assumption is necessary to account for the skewness of the pore distributions [21] in a system where the formed nuclei can only grow proportionally to a certain driving force and their areas. The parameter $\beta_1 = 1.2$ and $\beta_2 = 15$ were fitted to experimental pore distributions obtained from the analysis of scanning electron microscope (SEM) images of the dried product. The use of an exponential distribution, having only one parameter instead of two, was considered but the results were not satisfactory at all.

11

Using the Method of Characteristics (MoC) [22], an analytical solution of the above model can be derived, leading to

$$L = L_0 \exp\left\{ \int_{t_0}^{t_{end}} G'(t)dt \right\} \tag{24}$$

and

$$n = n_0 \exp\left\{ -\int_{t_0}^{t_{end}} G'(t)dt \right\} \tag{25}$$

Given an initial range of dimensions of the nuclei, their distribution, and a thermal profile, Eqs. (18) and (20) can be used to derive σ and G' that, according to Eq.(16) reads $G' = k_{cg}\sigma^g 2\pi\Delta z$. From G', the integral can be calculated and the crystal size distribution at time t_{end} can be determined. Since the infrared camera can provide the evolution of the whole axial temperature profile of the product, measurements from different pixels along the vial height can be used to predict the whole axial crystal size distribution.

If the whole temperature profile was provided, then t_0 is simply t_{ind} and t_{end} is the moment that the thermal equilibrium between the product and the environment has been reached. If measurements were provided at a given time step, e.g. every second, then the time evolution of the crystal size distribution could be monitored in real time. The computational effort is negligible, enabling the application of the proposed model to the on-line monitoring and optimization of the freezing step.

4. Case Study and Experimental Work

Freezing tests were performed in a laboratory-scale freeze-dryer (Lyo Beta by Telstar, Spain) and, in each batch, ten vials [10R (ISO 8362-1)] were filled with 5 ml of a 5% b.w. solution of sucrose. Chemicals were purchased from Sigma Aldrich ($\geq$99.5%) and used as received. Solutions were prepared with ultra-pure water produced using a Millipore water system (Milli-

12

Q RG, Millipore, Billerica, MA). Each test was 2.5 h long and the cooling policy was to simply cool to −50°C as fast as possible, that is, with a cooling rate of about −1.5°C/min from room temperature to −10°C, about −0.5°C/min from −10°C to −30°C and −0.3°C/min from −30°C to −50°C. The temperature is directly measured and used in the model, so deviation from this cooling profile does not affect the analysis procedures. The vials were placed inside the chamber and monitored using the sensor presented in Lietta et al. [33] based on infrared imaging. The sensor consists of a protective enclosure in plastic material housing an infrared camera, an RGB camera and all the electronics required to control its functioning, acquire the images, store the results and evaluate in real time the evolution of the process. The system was designed to be placed inside the drying chamber while accessed and controlled via wi-fi from the exterior. In this work only the thermal images have been used and will be discussed. Among the parameters that the user can vary there is the frame rate, expressed in terms of seconds between the acquisition of two subsequent thermal images. One new frame was acquired every 10 seconds. Experimental values of the induction times were obtained from the analysis of thermal profiles. In fact, given the temperature of the equilibrium freezing point, function of the kind of solute and of the solid fraction inside the solution, the saturation of the solution can be identified as the first moment the solution presents a temperature lower than the freezing temperature. Nucleation is characterized by a quick heat release that brings the solution back to the equilibrium freezing temperature after this was undercooled. The induction time was computed as the time elapsed between the saturation of the solution and the detection in a single frame of the sudden heat release due to nucleation

One more freezing test was carried out exactly in the same conditions, but the samples were also dried after being frozen. The temperature of the shelves and chamber pressure during the primary drying phase were set to $T_{sh} = −20°C$ and $P_c = 10$ Pa. The thermal evolution of the material was monitored using the same sensor described above. The dried material contained

in the two vials located in front of the camera was extracted from the vials, cut in slices at different axial positions, fixed on aluminum circular stubs, and metallized with chrome. SEM images (SEM, FEI type, Quanta Inspect 200, Eindhoven, The Netherlands) were taken along the axis of the vial in three different radial positions: at the center of the vial and at both edges where the product was in contact with the glass. The measurement at different radial positions allows the consideration of variability inside the vial; the thermal profiles obtained from the sensor refer to the temperature of the material in direct contact with the glass of the vial, which is thus associated with the pore size distribution forecast by our model. Significant differences would require a further correction of the temperature to account for the internal heat transfer. The images obtained were pretreated and segmented as discussed in Colucci et al. [21]. After segmentation, all the pores were counted, together with their areas and equivalent perimeters. The axial distribution of the pores is reported as an average of the values obtained from the two dried samples (two measurements for the distribution on the center of the vials and four for the measurement of the pores in contact with the glass). The error bars reported correspond to one standard deviation. No macroscopic collapse of the dried structure was visible, so the assumption that the distribution of the pores results from that of the ice crystals is reasonable.

The ending of the primary drying of this validation batch was experimentally determined from the analysis of the Pirani-Baratron ratio. The lab-scale equipment used for this work has embedded both a capacitance (Baratron type 626A, MKS Instruments, USA) and a thermal conductivity (Pirani type PSG-101-S, Inficon, Switzerland) manometer. The measurement of the Pirani gauge varies with the composition of the atmosphere inside the chamber, thus the pressure measurement will be about 60% higher than the actual pressure in the chamber read by the Baratron when sublimation is occurring, as the gauge is calibrated in air while the chamber atmosphere is about 100% water vapor. After drying is over, when no water vapor is left in the chamber, the two sensors will read the same pressure, that is, their ratio will be one.

14

Between these two values, the ratio presents two slope changes, namely the onset and offset, while the inflection point between the two is referred as the midpoint. Which of these points should be considered as end of the primary drying depends on the kind of products. For amorphous products like sucrose, the midpoint should be considered [34]. The maximum temperature at the sublimation interface was obtained from the analysis of the thermal images of the products.

5. Validation

Validation of the proposed model was performed at many levels. The main interest of any freeze-drying practitioner is the possibility to obtain a reliable prediction of the porous structure, that is, the resistance to mass transfer, thus the possibility to estimate the ending time and the maximum temperature during the primary drying phase for a given set of operating conditions (T_{sh} and P_c). For this reason, a first round of validation was performed with the aim to compare the pore size distribution forecast by the model with the experimental pore size distribution obtained from the analysis of the images of the product obtained from the Scanning Electron Miscroscope (SEM).

Simulation of the ending time and maximum product temperature at the sublimation interface were obtained using the one-dimensional model of the primary drying presented by Velardi and Barresi [35]. Despite of its simplicity, this model was proven effective for on-line application in many works presented after its publication. Two parameters must be provided to the model to simulate the process: the global heat exchange coefficient between the shelf and the product, K_v, and the mass transfer resistance coefficient R_p. The former is a characteristic of the vial-freeze-dryer system, thus completely independent from the actual formulation processed and can be accurately estimated off-line processing just a few vials filled with water. In this work, K_v was obtained by the gravimetric test [36]. The mass transfer coefficient R_p is

15

more challenging to estimate since it depends on the actual formulation processed and its porous structure. Following the approach presented in [37,38], it can be estimated from the average axial pore distribution. Here the pore distributions estimated from the previously discussed model of the freezing stage were used to estimate R_p according to

$$R_p = \sum_i R_{p,i} = \sum_i \frac{3}{2} \frac{\tau^2}{\xi} \frac{\Delta z}{\bar{D}_{p,i}} \sqrt{\frac{\pi RT}{2M_w}} \tag{26}$$

where $R_{p,i}$ is the mass transfer resistance in a slice of the product of height Δz, R is the ideal gas constant, M_w is the molar mass of water, and T the temperature in the dried layer, usually approximated by T_i, the temperature at the sublimation front, that is, the region where the vapor flow originates and propagates.

The ratio of the square of the tortuosity, τ, and of the porosity of the pore network, ξ, namely τ^2 / ξ is assumed equal to 0.225 according to [23]. The model presented in [35] assumes that, at any time instance, two layers can be distinguished inside the product: a frozen layer and a dried layer. Those two layers are separated by a perfectly flat sublimation interface receding uniformly towards the bottom of the vial. To be consistent with this simplified model of the process, the mean pore diameter $\bar{D}_{p,i}$ must be a single value that is spatially uniform across the ith slice. As a unique value is considered for each slice, the mean pore diameter $\bar{D}_{p,i}$ has only discrete variations along the product axis. All the models presented in the literature so far were just able to estimate, at a certain position along the product axis, an average value of the pore diameters, and this single value was enough to estimate R_p. In our case, the solution of the 1D-PBM provides the evolution of the pore size distribution along the axial direction. If we assume the product to be discretized according to the pixels of the camera that provides the thermal measurements, we obtain that, for each slice of the product, we can account for the increased information. Besides, since this pore distribution appears very skewed, the average

16

value does not guarantee to be the best characterization of the whole distribution. In this work, four different characterization of the crystal size distribution were compared:

i)   The average diameter, $\bar{D}_{p,i}^{1/0}$, obtained as the ratio between the first and the zeroth order moments of the distribution;

ii) The average diameter, $\bar{D}_{p,i}^{2/1}$, obtained as the ratio between the second and the first order moments of the distribution;

iii) The mode of the distribution, $\bar{D}_{p,i}^{m}$;

iv) Given the discretized histogram of the pore distribution inside the ith slice, that is, the probability p_j of having a pore of diameter $D_{p,ij}$, the average pore diameter $\bar{D}_{p,i}^{W}$ is the inverse of the sum over j of the ratios between p_j and $D_{p,ij}$.

Approach iv assumes that all the pores having a certain diameter will contribute to the total mass transfer according to their frequency, thus the total R_p for the ith slice will be the weighted sum of all single contributions $R_{p,ij}$ due to the pores having a diameter $D_{p,ij}$.

This rationale implies that

$$R_p = \sum_i \sum_j p_j R_{p,ij} = \sum_i \sum_j \frac{3}{2} \frac{\tau^2}{\xi} \Delta z \sqrt{\frac{\pi R T_i}{2 M_w}} \frac{p_j}{D_{p,ij}} \tag{27}$$

where T_i for each axial position i was measured from the sensor during the primary drying.

If Δz is kept constant, this equation simplifies to

$$R_p = \sum_i \frac{3}{2} \frac{\tau^2}{\xi} \Delta z \sqrt{\frac{\pi R T_i}{2 M_w}} \sum_j \frac{p_j}{D_{p,ij}}, \tag{28}$$

which is equivalent to Eq. (26) if the average diameter is defined by

$$\bar{D}_{p,i}^{W} = \frac{1}{\displaystyle\sum_j \frac{p_j}{D_{p,ij}}}. \tag{29}$$

17

The above model was developed to be coupled with real-time temperature measurements provided by an infrared camera developed as a Process Analytical Technology for monitoring and optimization of the freeze-drying process. In this perspective, the correct estimation of the crystal size distribution, as well as the possibility to infer the mass transfer coefficient important in the simulation of the subsequent primary drying, has a dramatic importance. One single freezing test might provide the information required to draw the whole design space of a specific formulation, if the information on the heat transfer coefficient during the primary drying inside the equipment is provided.

A further validation step was performed simulating the thermal evolution of the product during the whole freezing process. A more general model of the freezing of a 10R vial filled with 5 ml of a 5% b.w. sucrose solution was developed using a modified porous media approach. Fig. 1 presents the schematics of the system. Given the symmetry of the cylindrical vial, a 2D section was simulated. The details of the model are presented in Appendix A.

The model was solved by the finite volume method. A mesh of forty per twenty-five (five for glass and twenty for the product) cells was able to provide grid-independent results. Eleven classes where considered for the solution of the population balance while the time step was set to 0.05 s. Thermodynamic parameters, see Table 2, were taken from [43-45] for water, from [43] for ice and from [46] for sucrose.

6. Results

Fig. 2 reports the squared sum of errors for different values of the exponent of the nucleation kinetics, b. The absolute minimum corresponds to $b = 12$, although the difference with the values obtained for $b = 11$ and 13 is minor. Larger sets of observations might make this minimum more evident but, looking at Fig. 2, we could expect b to range from 9 to 14, in agreement with the primary nucleation mechanism. The resulting parity plot obtained from the

18

comparison of the experimental and simulated induction times, Fig. 3, shows a good agreement between the two set of values. A slight deviation from the diagonal can be observed on the left together with an increased variability in the estimations. In those vials, nucleation occurs earlier and would, for this group of observations only, be better described by a lower exponent. A possible reason for this small variation from the general trend could be that nucleation was enhanced by some other factor, e.g. impurities in the solution. As expected from the stochastic nature of the primary nucleation process, the variability in the induction times is large.

Koop et al. [47] claimed that the nucleation kinetics of water solution is not dependent on the kind of solute dissolved and, thus, whatever the formulation, the parameters that describe the nucleation kinetics should be the same. Following the procedure presented in this work, the accuracy of this claim could be tested by measuring the nucleation exponent for other sugars or more complicated solutions. If the value of the exponent b is the same, also k_b would be the same, that is, the only real difference in the resulting pore size distribution would be due to the crystal growth kinetics.

Much of the literature reports values of the growth order g of 1 or 2 depending on whether the crystal grows according to an *adhesive type* or a *spiral growth* mechanism [48]. A very good agreement with the experimental results was obtained for g equal to 1. The group $2\pi\Delta z k_{cg}$ was almost constant, that is k_{cg} was mostly constant for a given value of g, in all the cases, and values in the range 5 to 10 are satisfactory. In Fig. 4 the experimental number density function (*ndf*) obtained from one SEM image taken next to the bottom of the product is compared with the prediction from the proposed 1D-PBM. The two assumptions, that the nuclei are formed according to a beta distribution and that crystal growth is the only mechanism occurring after nucleation, seem to provide a reasonably good description of the physics of the system. Further validation of the assumptions would be useful, since other kinds of phenomena could provide a skewed distribution of the nuclei. For example, a quadratic, cubic, or some other super-linear

19

dependence of the growth rate on L in Eq. (15) would lead to an acceleration of the growth rate for bigger crystals, thus to the creation of a tail on the right side of the *ndf*. An analytical solution of the resulting 1D-PBM can be derived in many cases. Another option is that, for highly concentrated solutions, the molecular diffusion of the water molecules towards the crystals becomes rate controlling; on the contrary, in deriving the proposed model the implicit assumption that the process rate was controlled by the adhesion of the water molecule to the crystal surface was made. If molecular diffusion were rate limiting, the crystal growth rate would be proportional to L^{-1}, which would favor little crystals over the bigger crystals, pushing the original normal distribution to the left to obtain a skewed *ndf*.

Figure 5 compares the average pore diameter measured from the SEM images taken at the edges of the cake, where the product is in contact with the glass, and simulated using the temperature measurements extracted from 9 pixels along the vial height. The procedure presented by Van Bockstal et al. [49] was used to correct the effect of the vial glass on the temperature measured from the infrared camera; the corrected profiles were fed to the population balance presented in Section 3. The simulated values were obtained using $b = 12$; k_b = 10 m^{-3}s^{-1}K^{-b}; $g = 1$, and $2\pi\Delta z k_{cg} = 10$ s^{-1}, i.e. k_{cg} equal to 1592 m^{-1}s^{-1}, and the ratio between the first and the zeroth order moments of the normal distribution function was considered as the average pore diameter. The agreement is acceptable, and, in all cases, the predicted values fall inside the range described by the error bars obtained from the average of the four experimental measurements. Both the pore reduction at the bottom of the vial and the effect of cryoconcentration − a small decrement of the average pore diameter towards the top surface of the product − are well described by the proposed 1D-PBM.

Figure 6 compares the distribution of the average pore diameters, measured from the SEM images using the algorithm of Colucci et al. [21], at the center of the vial, that is, on the axis of the cylindrical product, and in the radial position, that is, where the product is in direct contact

20

with the glass. Along most of the vial, the average pore diameter measured in the radial position is a few microns greater than the measurement at the product axis. If we consider the variability of the pore distribution, see Fig. 4, this difference will hardly be significant. The effect on the effective mass transfer coefficient can be considered negligible. At the best of the authors' knowledge, this kind of comparison is here presented for the first time and has a dramatic importance for the development of the PAT. An infrared camera measures the temperature directly on the glass wall. The effect of heat transfer across the glass can be corrected mathematically thus providing a measurement of the temperature of the product in direct contact with the glass. If the difference in the radial crystal size distribution is not significant, that is, the gradients inside the liquid during cooling are negligible, and the freezing front is mostly flat, then the crystal distribution obtained directly from this measurement can be considered representative of the crystal distribution over the whole product. There is no need to further correct the measured temperature in order to account for the radial variability of the pores.

Figure 7A compares the Pirani Baratron ratio of one of the two primary drying cycles performed and the evolution of the position of the interface simulated for the four different kinds of average diameters presented in Section 4. The measured onset of the Pirani-Baratron is 25.4 h, while the offset is 38.9 h. The experimental maximum temperature at the interface was −32°C. Fig. 7B compares the actual average pore diameters resulting from each of the four approaches. Taking the mode of the distribution, blue line in Fig. 7A and blue circles in Fig. 7B, the primary drying is supposed to end in 32.6 h, while the simulated maximum temperature is −30.5°C. Using Eq. (29), the average pores are slightly bigger, resulting in a drying time of 29.8 h and a maximum temperature of exactly −32°C. Approaches *i* and *ii* estimated the larger sizes of the pores, thus the shortest drying times, 29.0 h and 28.4 h respectively, and the lowest values of the maximum temperature at the interface: −32.8°C and −32.6°C respectively.

21

Approach *iv* appears to provide the best representation of the actual system. Especially remarkable is the accuracy in the estimation of the maximum temperature. Taking the mode of the distribution might be more conservative, while the simple average diameter appears more prone to underestimate the drying time and maximum temperature. All considered, the proposed model appears to correctly predict the pore size distribution which will determine the rate of mass transfer during the primary drying process.

In order to further validate the system, the 2D model described in Appendix A was implemented in Matlab and solved numerically. The same values of b, k_b, g, and $2\pi\Delta z k_{cg}$ used for the solution of the simple 1D-PBM were used. In Figure 8 the axial pore distribution measured from the SEM images (black triangles) are reported in terms of average of the two measurements and standard deviation between the measurements. The experimental values are compared with the values obtained from the simulation. The agreement is qualitatively correct although not perfect, in particular, the pores diameters at the bottom of the vial appear to be somewhat overestimated. It has to be remarked that the maximum difference between the simulated and experimental profiles is 5μm: 5μm difference in the average computed on histograms ranging, as shown in Figure 4, between 20 and 180/200μm. These minor differences must be evaluated taking into account the uncertainties in both the sample preparation before the SEM analysis and the variability of the parameters of the algorithm for the analysis of this images, for the experimental results, and considering that the hypothesis behind the derivation of the model used for the simulation of the crystal size distribution discussed previously might affect the accuracy of the predictions. All these mild differences in the computed and experimental crystal size distribution will reflect in equivalent differences in their characterization, i.e. calculation of the averages.

Figure 9A compares the temperature measured from a thermocouple stuck inside the vial in close contact with the bottom of the vial and the temperature simulated for a cell in the right

22

bottom corner of the mesh. In blue is the temperature of the cooling medium. The agreement is outstanding along the whole process. Only a slight difference between the two values might be seen at the end when the material is mostly frozen. Same consideration stands for the temperature measured on the vial glass by the infrared camera. Figures 9B and 9C compare two measurements, obtained at the top and at the bottom of the vial, respectively, with the simulated values at the free side of the glass. The measurements of the IR camera were obtained using a value of glass emissivity of 0.93, measured at 0°C. The emissivity changes with the temperature which could explain, at least partially, the slight differences on the measurement obtained at the very beginning and end. Considering all the uncertainties in the measurements and in the simulation, the agreement is remarkable. One last validation of the presented model is the prediction of the sugar mass fraction in the solution at the end of the freezing. The glass transition temperature is defined to be the temperature at which, due to the increased viscosity of the solution, no further freezing can be observed in real time [50]. For a water-sucrose solution the glass transition is −32°C and corresponds to almost 20% of bound water, that is 20% of the total water remains bounded to the solid structure [50]. This value has a certain importance since this water will not be removed during the primary drying, except for a small fraction, but will need to be desorbed during the secondary drying phase. Since the driving force for crystal growth in our model is provided by the difference between the chemical potentials of ice and solution, this driving force will go to zero exactly when freezing is over. If the UNIQUAC model parameters have been correctly estimated, the freezing will be over when the glass transition temperature has been reached and the solute mass fraction is the one dictated by the thermodynamics of the system.

7. Conclusions

23

The possibility to monitor in real time the freezing stage of a pharmaceutical formulation enables the prediction of the axial crystal size distribution, which specifies the mass transfer resistance during the drying phase. A good estimation of this parameter, the most challenging one of the two required by simplified one-dimensional models of the process, opens a wide range of possibility and is expected to strongly boost the optimization and control of the whole freeze-drying cycle. A further step towards the implementation of a real quality-by-design approach to the manufacturing of pharmaceuticals and drugs. The possibility to use the thermal characterization of the product provided by an infrared camera was discussed in [21], in which past mathematical models from the literature were used to obtain a PAT for the monitoring of the vacuum freeze-drying process. Those models and the state-of-the-art methodology used to relate the thermal evolution of the process to the crystal diameters presented some issues and limitations. In this work, a new mathematical model that is more physically grounded and detailed was developed and validated, for the case study of a 5% b.w. sucrose solution. The proposed PAT uses the temperature directly measured from the sensor on the vial surface to model the nucleation and crystal growth kinetics. The infrared sensor can provide the evolution of the temperature in different position along the product height. From this profile it is possible to directly measure the nucleation temperature, that is the achieved degree of supercooling of the solution, thus the correct number of nuclei formed. Monitoring the temperature profile, it is also possible to model the crystal growth kinetics thus to infer the resulting crystal size distribution at the end of the freezing step. In fact, the driving force for crystal growth is the difference in the chemical potentials of the ice and of the solution and they can be correctly modelled and computed given a measurement of the product temperature. The results suggest a wider validation in the case of other sugars and more complex formulations should be carried out in future work.

24

Some authors have claimed that the nucleation kinetics in these systems are independent of the actual kind of solute. This claim should be tested in future work since it would have a dramatic impact in the future development of these kind of models by reducing the number of parameters of the presented 1D-PBM to one. On the other hand, if the solute does affect the nucleation kinetics, which may be probable for solutions of proteins, the actual dependence of these parameters from the characteristics of the solute must be studied.

Even if the nucleation kinetics were independent of the solute, the nucleation kinetics still presents many unknown aspects that the stochastic model here used does not fully explain. The speed at which nuclei formation propagates along the whole vial after the first crystal is observed, and the fact that the number density of crystals is mostly spatially uniform, suggest an unstable dendritic growth of crystals from the point where nucleation first occurs towards the other directions in space. Accurately describing such phenomenon would be a significant contribution to the mathematical modeling of freeze drying. The effects of the glass-solution interface or of the gases dissolved inside the solution to enhance the nucleation have also to be better understood.

Application and validation of this approach to the different kinds of controlled freezing processes, such as ice fog nucleation and vacuum-induced nucleation, is also one of the major future developments of this work since these methodologies are getting more and more important in the industrial practice.

8. Acknowledgements

Appendix A

The idea behind the porous media approach is that, although a system might be heterogeneous at the macroscopic level, for a sufficiently small part of the system, we might assume that its effective properties can be described as a linear combination of the properties of the single phases. If effective, averaged properties of the system can be derived, the typical transfer equation can be written and numerically solved in this discretized domain. The main difference with the more usual porous media approach is that ϕ does not define the fraction of the total volume occupied by the solid structure, but the volume fraction of the solute dissolved in the solution. The remaining $1 - \phi$ part of every cell can be either water or ice. With the saturation S_j defined as the volume fraction of either water or ice over the volume of everything apart from the solid, we can write

$$\phi + (1-\phi) S_i + (1-\phi) S_l = \phi + (1-\phi)(S_i + S_l) = 1 \tag{A.1}$$

$$S_i + S_l = 1 \tag{A.2}$$

The mass balance for ice and water respectively can then be described by

$$\frac{\partial S_i}{\partial t} = \frac{1}{(1-\phi)\rho_i} \dot{I} \tag{A.3}$$

$$\frac{\partial S_l}{\partial t} = \frac{\partial (1-S_i)}{\partial t} = -\frac{1}{(1-\phi)\rho_i} \dot{I} \tag{A.4}$$

to be solved according to the initial conditions:

$$t = 0, \, \forall r, z, \, S_i = 0 \quad \text{(and obviously } S_l = 1) \tag{A.5}$$

The heat transfer inside the single cells can be described by

$$\frac{\partial T}{\partial t} = \frac{1}{c_{p,eff}\rho_{eff}}\left[k_{eff}\left(\frac{1}{r}\frac{\partial}{\partial r}\left(r\frac{\partial T}{\partial r}\right)+\frac{\partial^2 T}{\partial z^2}\right)+\lambda \dot{I}\right] \tag{A.6}$$

where $\dot{I}$ is the volumetric freezing rate, i.e., the kilograms per second of water that, in a given volume, turn into ice. This value links the mass balances described by Eqs. (A.3) and (A.4) to the heat balance, and can be measured from the third moment of the number density function, obtained from the 1D-PBM that is solved together with the model:

$$\dot{I} = \frac{\partial c_i}{\partial t} = \rho_i k_{shape}\int_0^\infty 3n(L,t)L^2 G(L,t)dL = 3\rho_i k_{shape}G'(t)\int_0^\infty n(L,t)L^3 dL \tag{A.7}$$

In fact, the third moment of the normal distribution function is proportional to the volumetric fraction of crystals in the solution. The derivative of the third moment is thus proportional to the volume of water that in a given dt turns into ice. Multiplication of this quantity by the ice density gives the freezing rate, the parameter that couples the microscopic 1D-PBM in the space of characteristics to the macroscopic description of the mass and heat transfer inside the vial. At the time $t = 0$, the temperature uniformly assumes a value T_0.

The set of boundary conditions implemented:

$$t > 0, z = 0, 0 < r < R_g \qquad J\big|_{z=0} = K_v(T_{sh} - T\big|_{z=0}) \tag{A.8}$$

where K_v is the overall heat transfer coefficient that considers conduction and radiation within the gap between the vial bottom and the shelf surface and the conduction in the glass wall:

$$K_v = \left(\frac{s_{g,bottom}}{k_g} + \frac{1}{K_u}\right)^{-1}, \quad K_u = \frac{k_{air}(T_{air})}{l_{air}} + 4\sigma_b \varepsilon T_{av}^3 \tag{A.9}$$

$$J\big|_{z=H} = \sigma_b F_{sh,top}(T_{sh}^4 - T^4\big|_{z=H}) + \sigma_b F_{wall,top}(T_{wall}^4 - T^4\big|_{z=H}), \ t > 0, 0 < r < R_g, z = H \tag{A.10}$$

$$J\big|_{r=0} = 0, \quad t > 0, r = 0, \forall z, \tag{A.11}$$

At the top surface of the material, both radiation from the upper shelf and from the side wall were considered. The view factors were taken from [39,40].

27

The glass vial is mostly infrared opaque, having an approximate emissivity of 0.9, variable with temperature. For this reason, an infrared imaging system will read the temperature of the glass and not that of the product. The study of the dynamics of the glass wall is therefore important and was modeled and included in the two-dimensional model used for validation. In the glass, only heat transfer occurs, which is modeled by

$$\frac{\partial T_g}{\partial t} = \frac{k_g}{c_{p,g}\rho_g}\left(\frac{1}{r}\frac{\partial}{\partial r}\left(r\frac{\partial T}{\partial r}\right) + \frac{\partial^2 T}{\partial z^2}\right) \tag{A.12}$$

which is solved with the initial condition:

$$T_g = T_0 \; t = 0, \forall r, z \tag{A.13}$$

The boundary conditions that describe conduction and radiation at the vial wall, together with the direct conduction between the glass and the shelf, are

$$J\big|_{r=R_g+s_g} = h_{side}(T_{air} - T_g\big|_{r=R_g+s_g}) + \sigma_b \, \mathrm{F}_{sh,side}(T_{sh}^4 - T_g^4\big|_{r=R_g+s_g}) + \sigma_b \, \mathrm{F}_{wall,side}(T_{wall}^4 - T_g^4\big|_{r=R_g+s_g}),$$

$$t > 0, r = R_g + s_g, \forall z \tag{A.14}$$

$$J\big|_{z=0} = K_c(T_{sh} - T_g\big|_{z=0}), \;\; t > 0, z = 0, R_g < r < R_g + s_g \tag{A.15}$$

where h_{side} was taken from [41] and K_c, here considered as an effective heat transfer coefficient modeling also the effects of the heat transfer in the radial direction inside the glass at the bottom of the vial, was taken from [42].

Given the difficulties in estimating the contribution of radiation from the remaining walls of the vial not modeled, this was assumed similar to the radiative terms used to model the top surface of the product, thus

$$J\big|_{z=H} = \sigma_b \, \mathrm{F}_{sh,top}(T_{sh}^4 - T_g^4\big|_{z=H}) + \sigma_b \, \mathrm{F}_{wall,top}(T_{wall}^4 - T_g^4\big|_{z=H}), t > 0, R_g < r < R_g + s_g, z = H$$

$$\tag{A.16}$$

In addition, at any moment, the energy flux transferred through the glass was assumed equal to the heat received by the product:

28

$$k_g \left. \frac{\partial T_g}{\partial r} \right|_{r=R_g} = k_{eff} \left. \frac{\partial T}{\partial r} \right|_{r=R_g} , \quad \forall t, r = R_g, \forall z \tag{A.17}$$

9. List of Symbols

a_{ijk}	Interaction coefficients in the UNIQUAC model	Different units
a_w	Activity coefficient	-
$A_{crystal}$	Crystal surface area	
b	Crystal nucleation order	-
B	Beta probability distribution modeling the nuclei's size	m^{-1}
B_0	Volumetric nucleation rate	# m^{-3} s^{-1}
c_i	Ice concentration	kg m^{-3}
c_p	Specific heat capacity	J $kg^{-1}K^{-1}$
$\bar{D}_{p,i}$	Average pore diameter	m
f	Probability distribution function Master Equation	s^{-1}
$F_{1,2}$	View factor between surface 1 and surface 2	-
g	Growth rate order	-
$G(L,t)$	Growth rate	m s^{-1}
$G'(t)$	Growth frequency as defined in Eq.(16)	s^{-1}
ΔH_{fus}	Latent heat of fusion	J kg^{-1}
h	Heat transfer coefficient	J s^{-1} m^{-2} K
H	Liquid height	m
$\dot{I}$	Freezing rate	kg $m^{-3}s^{-1}$
J	Heat flux	J $s^{-1}m^{-2}$
k	Thermal conductivity	J $s^{-1}K^{-1}m^{-1}$
k_b	Kinetic parameter for crystal nucleation	m^{-3} s^{-1} K^{-b}
K	Nucleation rate	# s^{-1}
K_c	Heat transfer coefficient for conduction from the shelf to the glass	J s^{-1} $m^{-2}K^{-1}$
K_u	Global heat transfer coefficient from the shelf and the vial bottom	J s^{-1} $m^{-2}K^{-1}$
K_v	Global heat transfer coefficient from the fluid and the product bottom	J s^{-1} $m^{-2}K^{-1}$
k_{cg}	Kinetic parameter for crystal growth	m^{-1} s^{-1}
k_{shape}	Particle shape factor	-
l_{air}	Average gap between the vial and the shelf	m
L	Particle characteristic dimension	m
L_{frozen}	Thickness of the frozen layer	m
$L(k_b \vert t_i)$	Likelihood of k_b being the exact parameter fitting the distribution given the measurement t_i.	s^{-i}
m	Mass	kg
M_w	Water molar mass	kg mol^{-1}
n	Number density function	m^{-4}

N	Number of observations for nucleation parameters optimization	-
p_j	Probability of having a pore of diameter $D_{p,ij}$, that is the j-th bin of the i-th section of the vial	m^{-1}
P	Velocity of the freezing front	ms^{-1}
P_c	Chamber pressure	Pa
q_i	Molecular surface area parameter	-
Q	Thermal gradient inside the frozen layer	$K\,m^{-1}$
r	Radial coordinate	m
r_i	Parameters of the UNIQUAC model	-
R	Ideal gas constant	$J\,mol^{-1}K^{-1}$
R_g	Vial inner radius	m
R_p	Mass transfer resistance during primary drying	ms^{-1}
$R_{p,i}$	Mass transfer resistance during primary drying in the i-th axial slice of the prodict	ms^{-1}
s	Integration variable	s
s_g	Vial wall thickness	m
$s_{g,bottom}$	Vial bottom thickness	m
S_j	Saturation	$m^3_j\,m^{-3}_{void}$
t	Time	s
t_{ind}	Induction time	s
T	Temperature	K
T^*	Liquid temperature	K
T_1^0	Fusion temperature of pure water	K
T_B	Temperature of the product at the bottom of the vial	K
T_f	Freezing temperature	K
T_i	Temperature at the sublimation interface	K
V	Liquid volume	m^3
w_i	Mass fraction	-
x_i	Molar fraction	-
z	Axial coordinate	m

Greek letters

α	Fitting parameter used to relate the thermal evolution of the process to the average pore diameter in Eq.(1)	$m\,K^{\beta}\,s^{-\beta}$
α'	Fitting parameter used to relate the thermal evolution of the process to the average pore diameter in Eq.(2)	$m\,K^{0.5}\,s^{-0.5}$
β	Fitting parameter Eq. (1)	-
β_1, β_2	Parameters of the beta distribution	-
γ	Activity coefficient	-
Δ	Finite difference	
ε	Emissivity	-
θ	Surface area fraction	-
λ	Latent heat of crystallization	$J\,kg^{-1}$
λ_1, λ_2	Parameters of Eq. (2)	-
μ	Chemical potential	$J\,mol^{-1}$
ρ	Density	$kg\,m^{-3}$
σ	Supersaturation	-

30

σ_0	Variance of the initial crystals pore distribution	
σ_b	Stefan-Boltzman constant	$J\ s^{-1}\ m^{-2}\ K^{-4}$
$\tau^2\big/\xi$	Parameter of Eq. (26)	-
τ_{ij}	Boltzman factor for residual excess Gibbs energy	-
ϕ	Volume fraction of solute dissolved	$m^3_{sol}\ m^{-3}_{cell}$
Ψ_b	Objective function	-
ω_i	Volume fraction of component i UNIQUAC	-

Subscripts

0	Initial value
air	Air in the drying chamber
av	Average value
bot	Vial bottom
eff	Effective value for the mix
frozen	Relative to the frozen product
g	Vial glass
i	Ice
l	Liquid
s	Solid
sat	Saturation
sh	Shelf
side	Vial side
top	Product upper surface
w	Water
wall	Camber wall

10. References:

[1] J. D. Mellor, *Fundamentals of Freeze-drying*. Academic Press: London, 1978.

[2] T.A. Jennings, *Lyophilization: Introduction and Basic Principles*; Interpharm/CRC Press: Boca Raton, 1999.

[3] G.W. Oetjen, P. Haseley, *Freeze-drying*. Wiley-VHC: Weinheim, 2004.

[4] D. Fissore, *Freeze-drying of pharmaceuticals*, in: Swarbrick J (Ed.), Encyclopedia of Pharmaceutical Science and Technology, 4th Edition. CRC Press, London, pp. 1723-1737, 2013.

[5] A. Hottot, S. Vessot, J. Andrieu, Freeze-drying of pharmaceuticals in vials: Influence of

freezing protocol and sample configuration on ice morphology and freeze-dried cake texture. Chem. Eng. Process. 46(7) (2007) 666-674. https://doi.org/10.1080/07373930600626388.

[6] J.C. Kasper, W.F. Friess, The freezing step in lyophilization: Physico-chemical fundamentals, freezing methods and consequences on process performance and quality attributes of biopharmaceuticals. Eur. J. Pharm. Biopharm. 78(2) (2011) 248-263.

[7] J. Searles, J. Carpenter, T. Randolph, The ice nucleation temperature determines the primary drying rate of lyophilization for samples frozen on a temperature-controlled shelf. J. Pharm. Sci. 90(7) (2001) 860-871. https://doi.org/10.1002/jps.1039

[8] I. Oddone, A.A. Barresi, R. Pisano, Influence of controlled ice nucleation on the freeze-drying of pharmaceuticals products: The secondary drying step. Int. J. Pharm. 524(1-2) (2017) 134-140. https://10.1016/j.ijpharm.2017.03.077

[9] B.S. Bhatnagar, M.J. Pikal, H.B. Robin, Study of the individual contributions of ice formation and freeze-concentration on isothermal stability of lactate dehydrogenase during freezing. J. Pharm. Sci. 97(2) (2008) 798-814. https://doi.org/10.1002/jps.21017

[10] W.B. Bald, Ice crystal growth in idealized freezing system, in Bald, W.B. (Ed.), Food Freezing, 1st edition (Chapter 5). Springer-Verlag, London, UK, pp. 67–80, 1991.

[11] J.L. Bomben, C.J. King, Heat and mass transport in the freezing of apple tissue. Int. J. Food Sci. Technol. 17(5) (1982) 615–632. https://doi.org/10.1111/j.1365-2621.1982.tb00221.x

[12] D.S. Reid, Cryomicroscope studies of the freezing of model solutions of cryobiological interest. Cryobiol. 21(1) (1984) 60–67. https://doi.org/10.1016/0011-2240(84)90023-3

[13] B. Woinet, J. Andrieu, M. Laurent, S.G. Min, Experimental and theoretical study of model food freezing. Part II. Characterization and modelling of the ice crystal size. J. Food. Eng 35(4) (1998) 395–407. https://doi.org/10.1016/S0260-8774(98)00036-3

[14] W. Kurz, D.J. Fisher, *Fundamentals of Solidification*, Trans Tech Publications, Switzerland, 1992.

[15] M. Kochs, C.H. Korber, I. Heschel, B. Nunner, The influence of the freezing process on vapour transport during sublimation in vacuum freeze-drying. Int. J. Food Sci. Technol. 34(9) (1991) 2395-2408. https://doi.org/10.1016/0017-9310(91)90064-L

[16] K. Nakagawa, A. Hottot, S. Vessot, J. Andrieu, Modeling of freezing step during freeze-drying of drugs in vials. AIChE J. 53(5) (2007) 1362-1372. https://doi.org/10.1002/aic.11147

[17] S. Bosca, A.A. Barresi, D. Fissore, Design of a robust soft-sensor to monitor in-line a freeze-drying process. Drying Technol. 33(9) (2015) 1039-1050. https://doi.org/10.1080/07373937.2014.982250

[18] S. Bosca, A.A. Barresi, D. Fissore, On the robustness of the soft sensors used to monitor a vial freeze-drying process. Drying Technol. 35(9) (2017) 1085-1097, https://doi.org/10.1080/07373937.2016.1243553

[19] R. Pisano, L.C. Capozzi, Prediction of product morphology of lyophilized drugs in the case of Vacuum Induced Surface Freezing. Chem. Eng. Res. Des. 125 (2017) 119-129.

[20] A. Arsiccio, A.A. Barresi, R. Pisano, Prediction of ice crystal size distribution after freezing of pharmaceutical solutions. Crys. Growth Des. 17 (2017) 4573-4581.

[21] D. Colucci, R. Maniaci, D. Fissore, Monitoring of the freezing stage in a freeze-drying process using IR thermography. Int. J. Pharm. 566 (2019) 488-499. https://doi.org/10.1016/j.ijpharm.2019.06.005

[22] P. Marchal, R. David, J.P. Klein, J. Villermaux, Crystallization and precipitation engineering—I. An efficient method for solving population balance in crystallization with agglomeration. Chem. Eng. Sci. 43 (1988) 59–67.

33

[23] L.C. Capozzi, R. Pisano, Looking inside the 'black box': Freezing engineering to ensure the quality of freeze-dried biopharmaceuticals. Eur. J. Pharm. Biopharm. 129 (2018) 58-65.

[24] F. Izmailov, A.S. Myerson, S. Arnold, A statistical understanding of nucleation. J. Cryst. Growth. 196 (1999) 234-242.

[25] O. Galkin, P.G. Vekilov, Direct determination of the nucleation rates of protein crystals. J. Phys. Chem. B. 103 (1999) 10965-10971.

[26] R.D. Dombrowski, J.D. Litster, N.J. Wagner, Y. He, Crystallization of alpha-lactose monohydrate in a drop-based microfluidic crystallizer, Chem. Eng. Sci. 62(17) (2007) 4802-4810

[27] L. Goh, K. Chen, V. Bhamidi, G. He, N.S. Kee, P.J.A. Kenis, C.F. Zukoski, R.D. Braatz, A stochastic model for nucleation kinetics determination in droplet-based microfluidic system. Crys. Growth Des. 10 (2010) 2515-2521.

[28] A.S. Myerson, *Handbook of Industrial Crystallization*, second Edition. Butterworth-Heinemann, Boston, Massachusetts, 2002, p. 144.

[29] H.M. Hulburt, S. Katz, Some problems in particle technologies. A statistical mechanical formulation. Chem. Eng. Sci. 19 (1964) 555-574.

[30] A.D. Randolph, M.A. Larson, *Theory of Particulate Processes: Analysis and Techniques of Continuous Crystallization*, Academic Press, Inc., New York, 1988.

[31] H.R. Corti, C.A. Angell, T. Auffret, H. Levine, H. M.P. Buera, D.S. Reid, Y.H. Roos, L. Slade, Empirical and theoretical models of equilibrium and non-equilibrium transition temperatures of supplemented phase diagrams in aqueous systems. Pure Appl. Chem. 80 (2010) 1065-1097.

[32] M. Catté, C.G. Dussap, C. Achard, J.B. Gros, Excess properties and solid-liquid equilibria for aqueous solution of sugar using a UNIQUAC model. Fluid Ph. Equilibria 96 (1994) 33-50.

[33] E. Lietta, D. Colucci G. Distefano D. Fissore, On the use of IR thermography for monitoring a vial freeze-drying process. J. Pharm. Sci. 108 (2019) 391-398.

[34] S.M. Patel, T. Doen, M.J. Pikal, Determination of end point of primary drying in freeze-drying process control. AAPS PharmSciTech. 11(1) (2010) 73-84. https://doi.org/10.1208/s12249-009-9362-7

[35] S.A. Velardi, A.A. Barresi, Development of simplified models for the freeze-drying process and investigation of the optimal operating conditions. Chem. Eng. Res. Des. 87(1) (2008) 9-22. https://doi.org/10.1016/j.cherd.2007.10.007

[36] R. Pisano, D. Fissore, A.A. Barresi, Heat transfer in freeze-drying apparatus, in dos Santos Bernardes, M. A. (Ed.), *Developments in Heat Transfer*, Chapter 6, 91-114. InTech, Rijeka (Croatia), 2011. https://doi.org/10.5772/23799

[37] N.F.H. Ho, T.J. Roseman, Lyophilization of pharmaceutical injections: Theoretical physical model. J. Pharm. Sci. 68 (1979) 1170–1174. https://doi.org/10.1002/jps.2600680930

[38] D. Fissore, R., Pisano, Computer-aided framework for the design of freeze-drying cycles: Optimization of the operating conditions of the primary drying stage. Processes 3(2) (2015) 406-421. https://doi.org/10.3390/pr3020406

[39] K. Gan, R. Bruttini, R. Crosser, A. Liapis, Heating policies during the primary and secondary drying stages of the lyophilization process in vials: Effects of the arrangement of vials in clusters of square and hexagonal arrays on trays. Drying Technol. 22(7) (2004) 1539-1575.

[40] K. Gan, R. Bruttini, R. Crosser, A. Liapis, Lyophilization in vials on trays: Effects of tray side. Drying Technol. 23(1-2) (2005) 341-363.

[41] F. Napoletano, Mathematical Modeling of the Freezing Process for Parenteral Products, Laurea Magistrale Thesis, Politecnico di Torino, Italy, 2016.

[42] W.Y. Kuu, S.L. Nail, G, Sacha, Rapid determination of vial heat transfer parameters using tunable diode laser absorption spectroscopy (TDLAS) in response to step-changes in pressure set-point during freeze-drying. J. Pharm. Sci. 98 (2009) 1136–1154.

[43] H. Sippola, P. Taskinen, Activity of supercooled water on the ice curve and other thermodynamic properties of liquid water up to the boiling point at standard pressure. J. Chem. Eng. Data. 63 (2018) 2986-2998.

[44] J.W. Biddle, V. Holten, J.V. Sengers, M.A. Anisimov, Thermal conductivity of supercooled water. Phys. Rev. E. 87 (2013) 042302.

[45] O. Benchikh, D. Fournier, A.C. Boccara, J. Teixeira, Photothermal measurement of the thermal conductivity of supercooled water. J. Phys. 46 (5) (1985) 727-731.

[46] R. Pongsawatmanit, O. Miyawaki, T. Yano, Measurement of the thermal conductivity of unfrozen and frozen food materials by a steady state method with coaxial dual cylinder apparatus. Biosci. Biotech. Biochem. 57(7) (1993) 1072-1076.

[47] T. Koop, B. Luo, A. Tsias, T. Peter, Water activity as the determinant for homogeneous ice nucleation in aqueous solutions. Nature 406 (2000) 611-614.

[48] T. Sowoidnich, A study of retarding effects on cement and tricalcium silicate hydration induced by superplasticizers, Ph.D. thesis, Bauhaus Universität Weimar, Germany, 2016

[49] P.J. Van Bockstal, J. Corver, L. De Meyer, C. Vervaet, T. De Beer. Thermal imaging as a noncontact inline process analytical tool for product temperature monitoring during continuous freeze-drying of unit doses. Anal. Chem. 90 (22) (2018) 13591–13599. https://doi.org/10.1021/acs.analchem.8b03788.

[50] F. Franks, T. Auffret, *Freeze-drying of Pharmaceuticals and Biopharmaceuticals: Practice and Principles*. RCS Publishing, Cambridge, UK, 2007.

List of Tables

Table 1. UNIQUAC parameters taken from [32].

Table 2. Thermodynamic parameters used for the simulation of the freezing of a vial filled with a solution of sucrose 5% b.w, taken from [43-46].

List of Figures

39

pore size distribution, i.e. $\bar{D}_{p,i}^{W}$; Red line: axial distribution of the ratio between the first and the zeroth moment of the pore *ndf*: $\bar{D}_{p,i}^{1/0}$; Green line: axial distribution of the ratio between the second and the first moment of the pore *ndf*: $\bar{D}_{p,i}^{2/1}$. B) Pore diameter used to measure R_p. Blue circles: $\bar{D}_{p,i}^{m}$; Gray triangles: $\bar{D}_{p,i}^{W}$; Red squares: $\bar{D}_{p,i}^{1/0}$; Green diamonds: $\bar{D}_{p,i}^{2/1}$.

Figure 8. Comparison between the experimental and simulated pore distribution at the center of the vial. Black triangles: experimental distribution obtained from the segmentation of the SEM images; Open circles: simulated average (ratio between the first and the zeroth moment of the *ndf* of the pore axial distribution: $\bar{D}_{p,i}^{1/0}$) pore diameter obtained from the 2D simulation of the freezing.

Figure 9. Comparison of the simulated temperature of the solution at the bottom of the vial (A), red solid line, and the one experimentally measured by a thermocouple (♦). Comparison of the simulated temperature, red solid lines, of the glass at the top (B) and at the bottom (C) of the vial and those measured using the IR camera at the top (▲) and at the bottom (▼) of the vial respectively. Blue solid line: temperature of the cooling fluid.

Figure 1
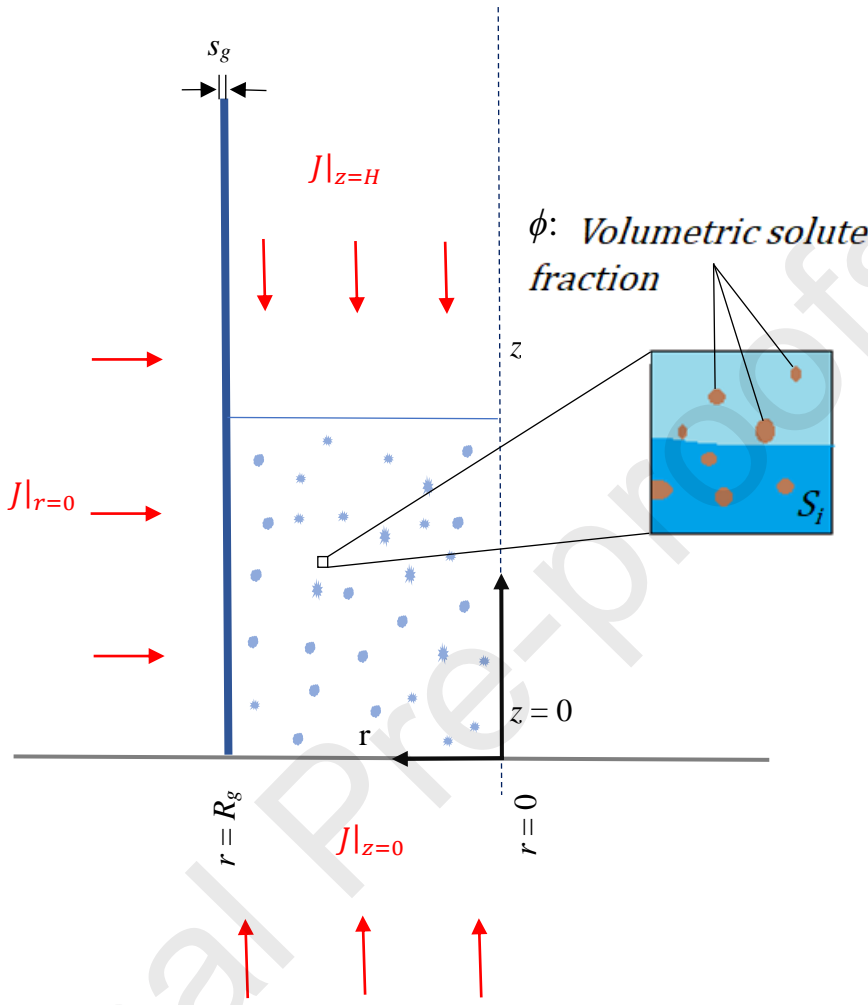
Figure 2
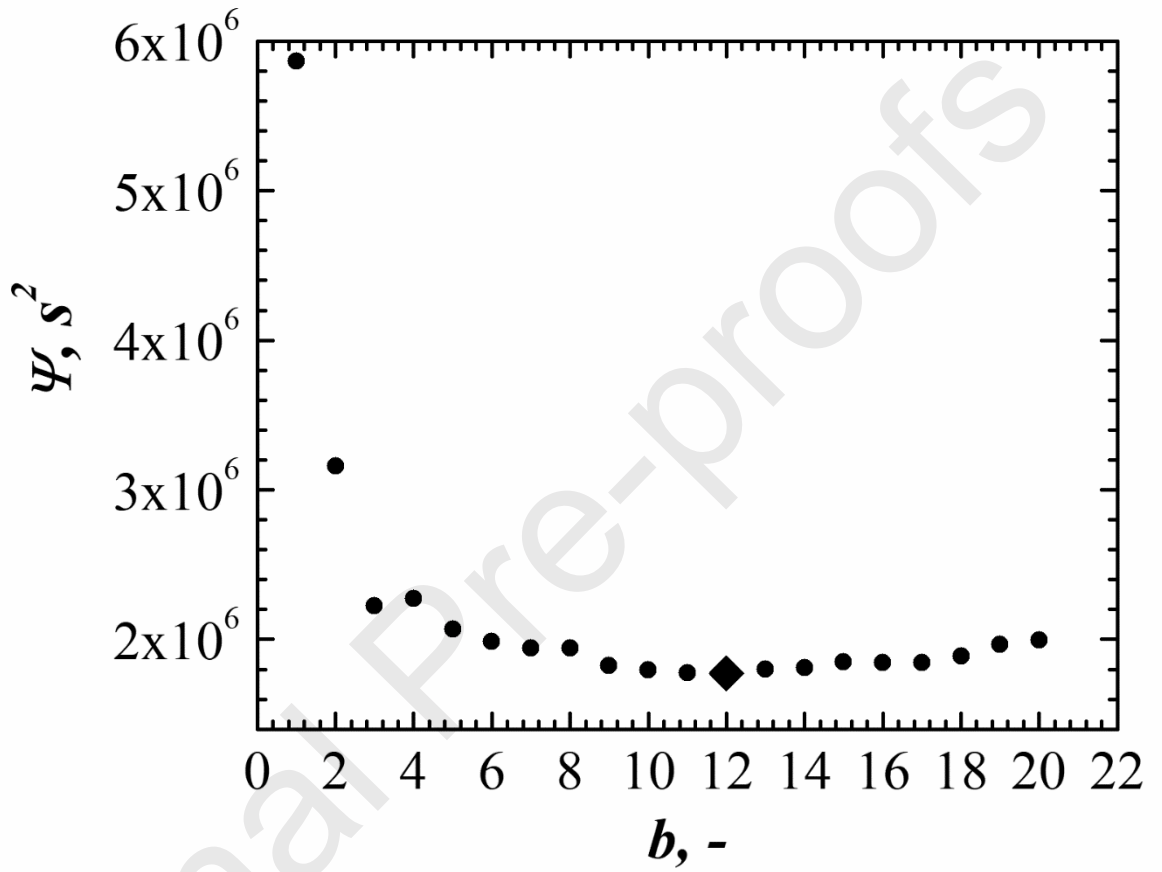
Figure 3
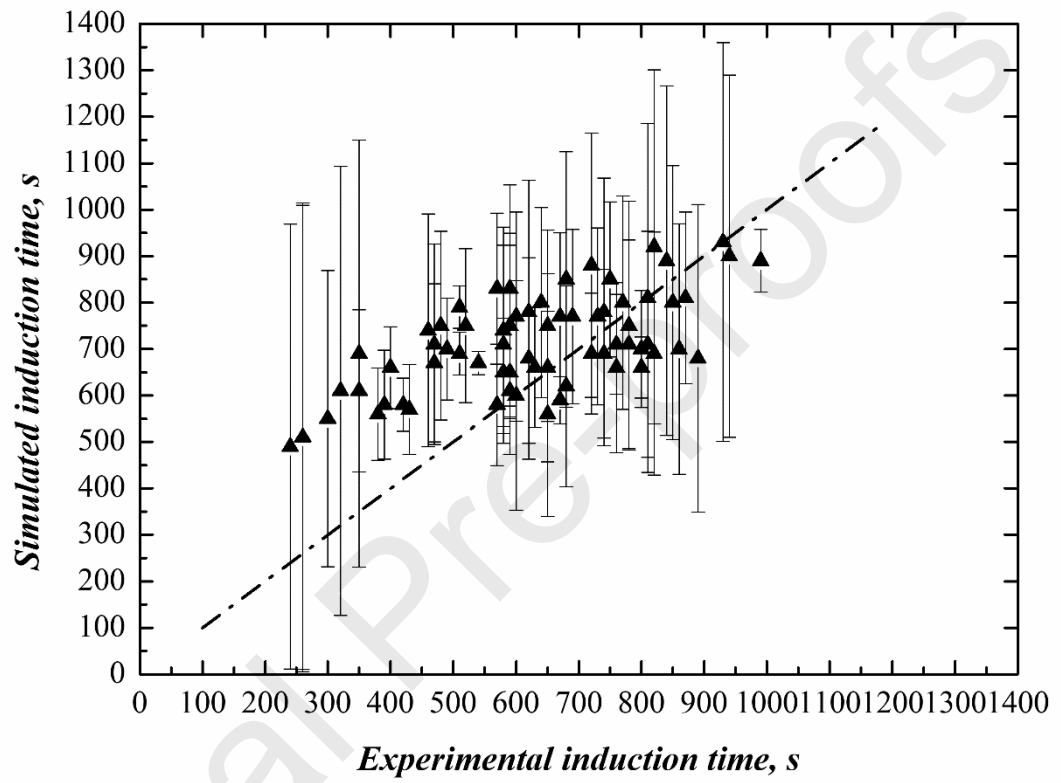
Figure 4
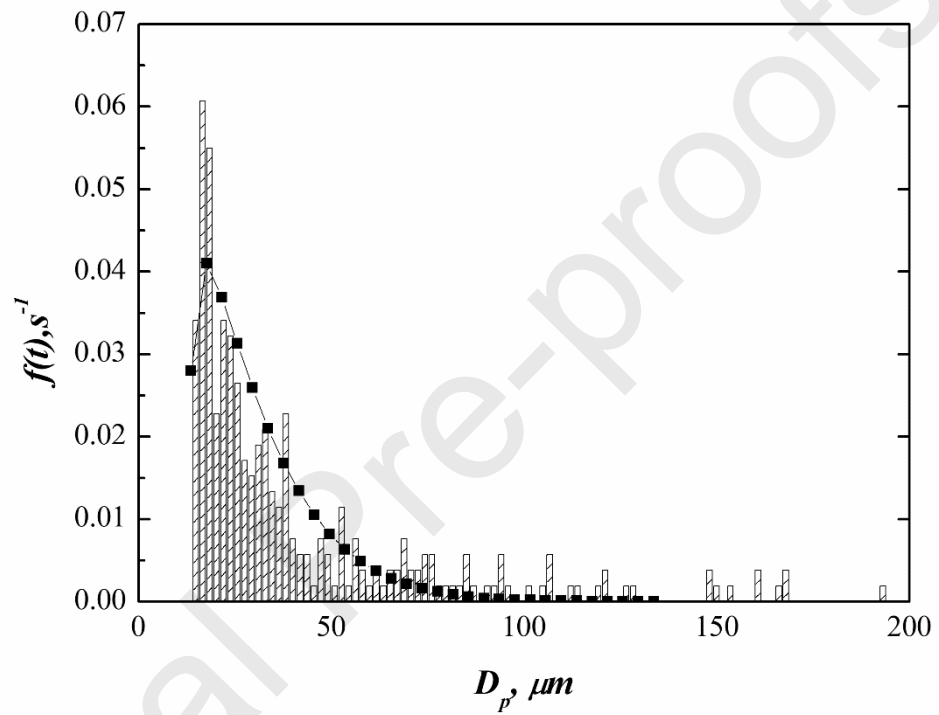
Figure 5

45
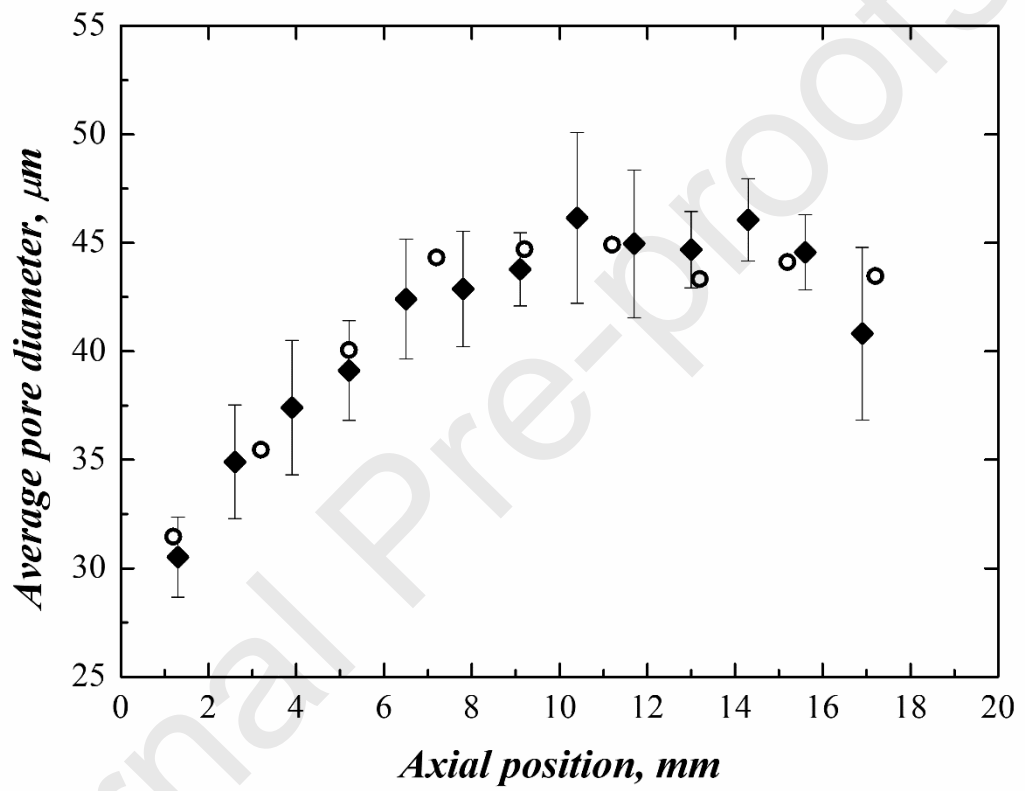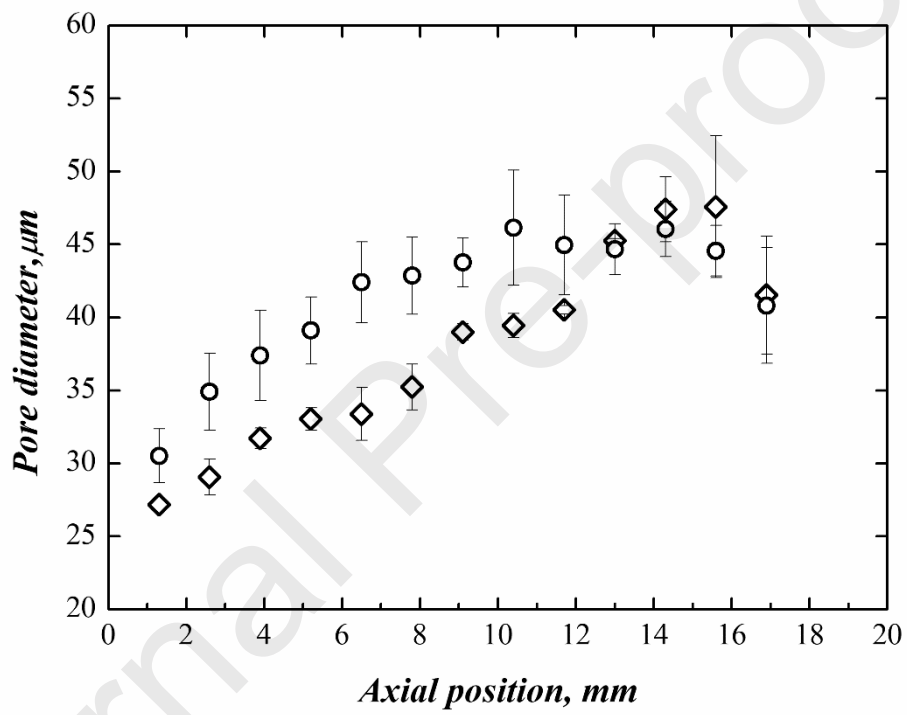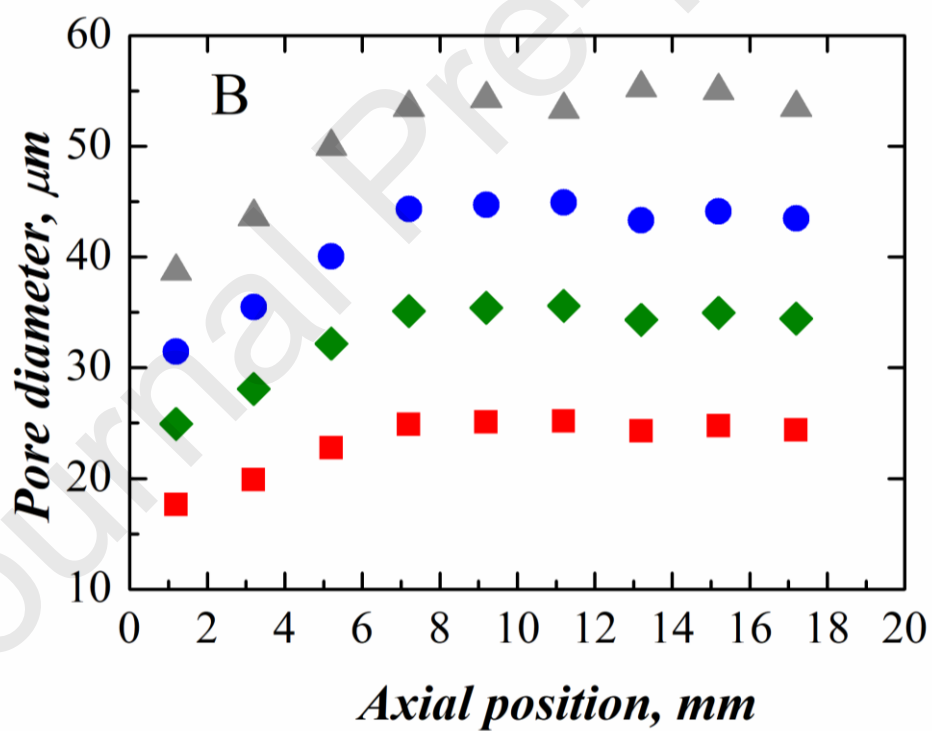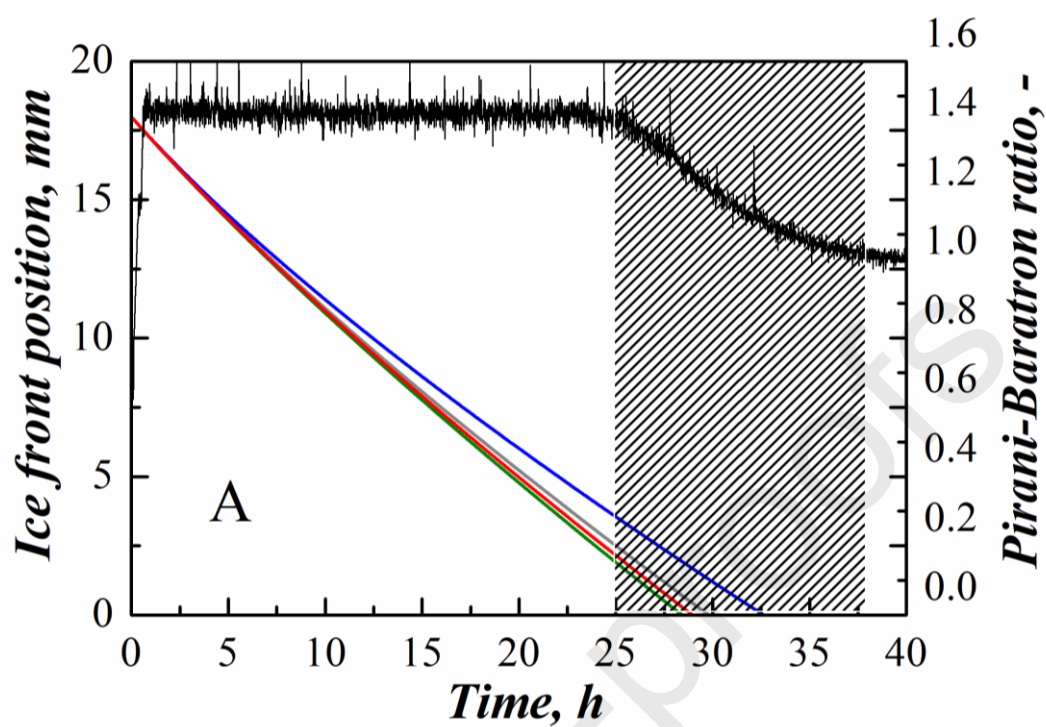
Figure 6

Figure 7

Figure 8
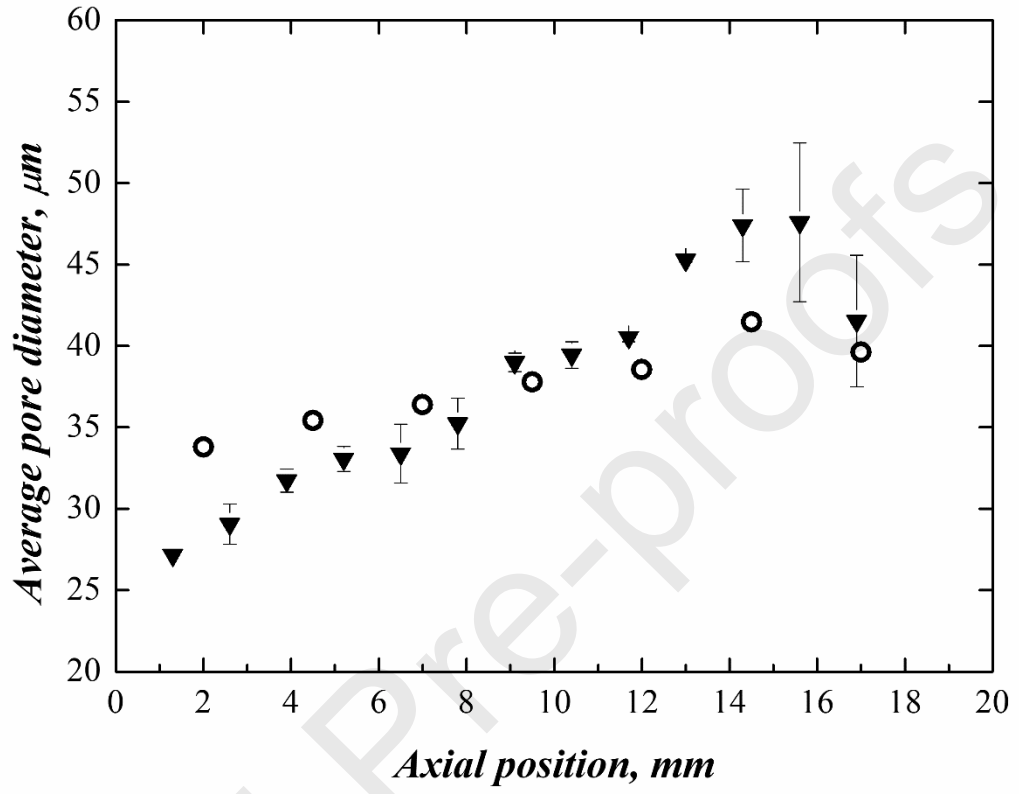
Figure 9
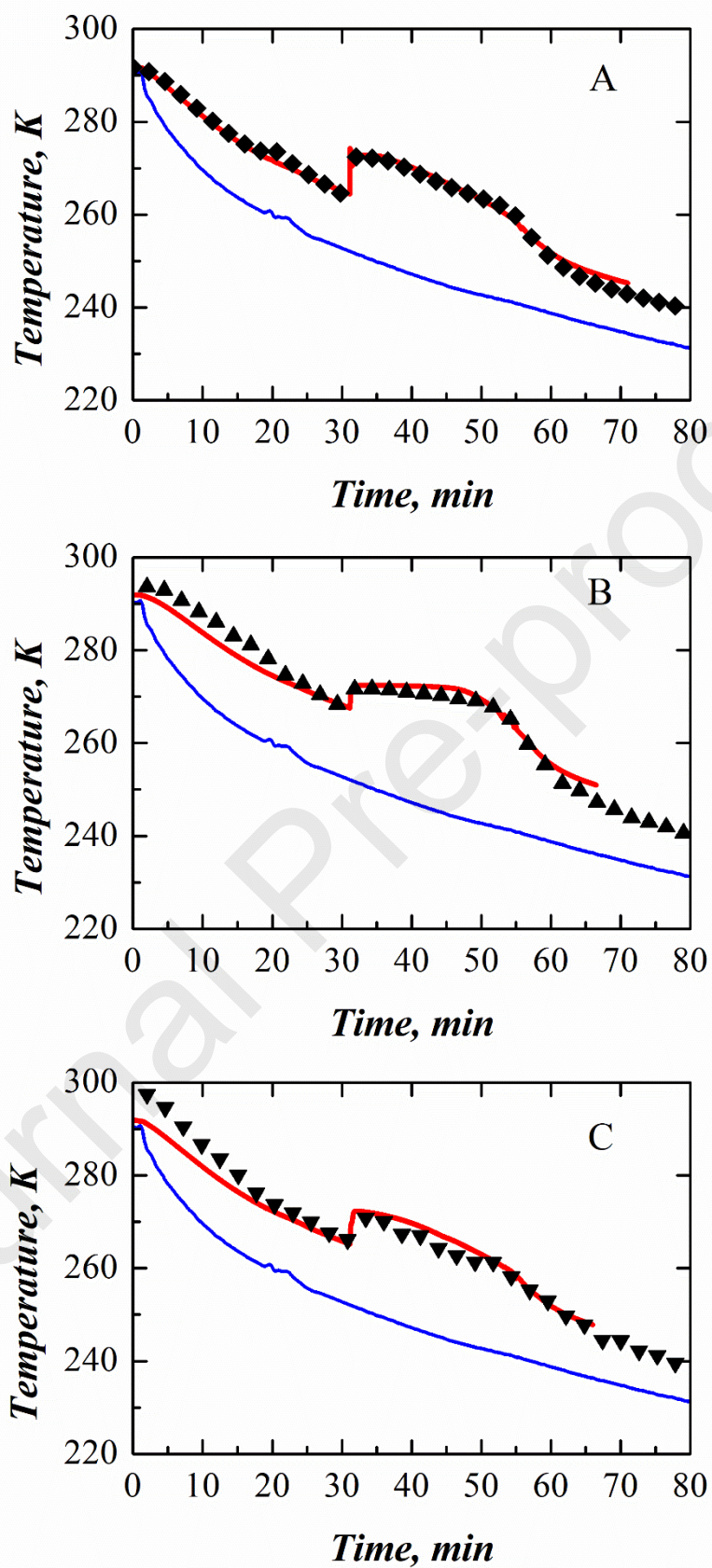
Table 1

	r_i	q_i	a_{ij1}	a_{ij2}	a_{ij3}
Water	0.92	1.40	92.69	−0.55	−0.59
Sucrose	14.55	14.31	−69.68	−0.56	−0.75

Table 2

	k, $\mathrm{Wm^{-1}K^{-1}}$	c_p $\mathrm{Jkg^{-1}K^{-1}}$	ρ, $\mathrm{kgm^{-3}}$
Glass	1.2	830	2230
Sucrose	0.29	1240	1587.9
Ice	$2.21 - 0.12 \cdot T$	$(2.12 + 0.008 \cdot T) \cdot 10^3$	$917 - 0.0137 \cdot T$
Water*	$0.75 \cdot \delta^{0.19}$	$55.5 \cdot (-19654.2 + 98.6 \cdot T - 0.14 \cdot T^2 + 2.3 \cdot 10^8 / T^2)$	$1007.9 \cdot \exp(-T_{crit} \cdot (3.97 \cdot 10^{-4} + 1.68 \cdot 10^{-3} \cdot \delta + 2 \cdot (-7.8 \cdot 10^{-4}) \cdot \delta^{0.5}))$

*$\delta = T/T_{crit} - 1$; $T_{crit} = 228K$

Nucleation and growth kinetics

Ψ, s^2

$b, -$

Temperature measurement

Temperature, K

Time, min
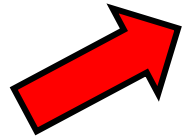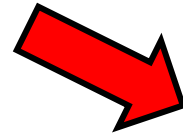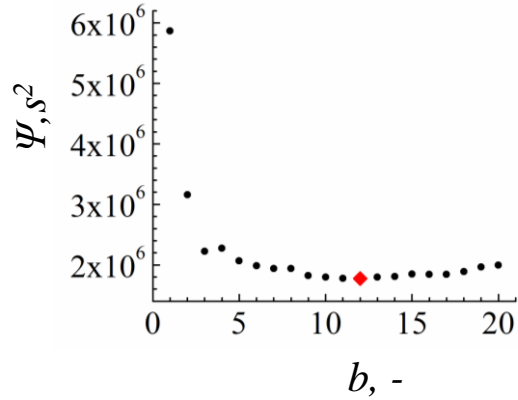
Mathematical model (1D-PBM)

Pore distribution

$f(t), s^{-1}$

$D_p, \mu m$
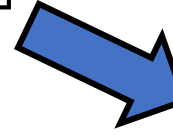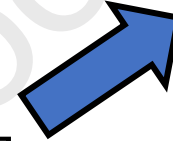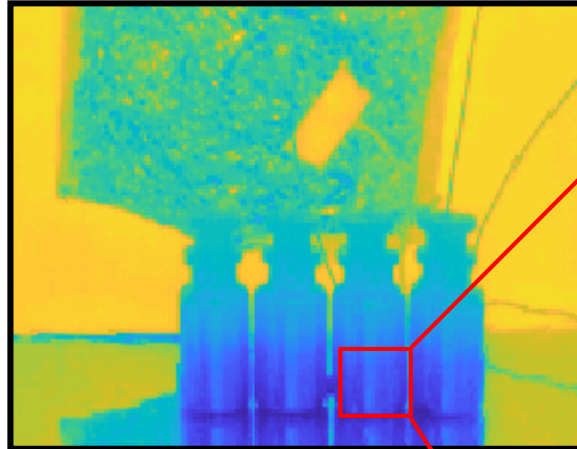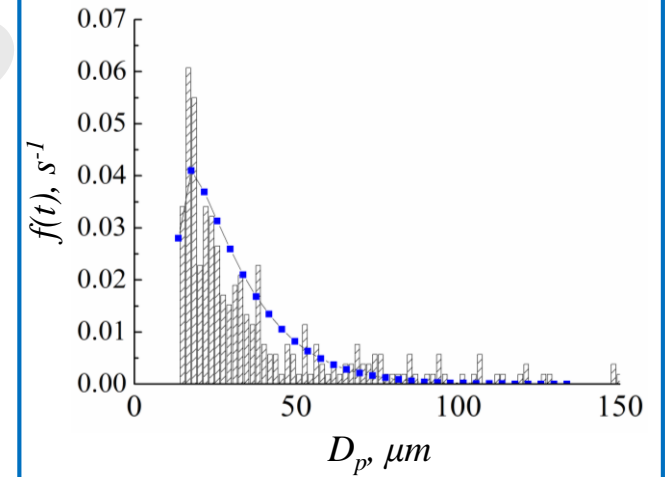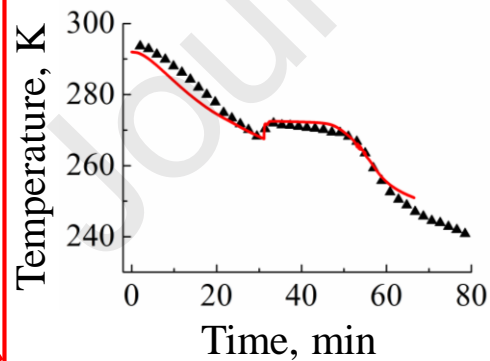
Primary drying simulation

Ice front position, mm

Pi/Ba ratio, -

Time, h